Experimental investigation on axial compressive behavior of novel FRP-ECC-HSC composite short column

Shuai Li, Tak-Ming Chan*, Ben Young

Department of Civil and Environmental Engineering, The Hong Kong Polytechnic University, Hong Kong, China

*Corresponding author.

Email address: tak-ming.chan@polyu.edu.hk (T.-M. Chan).

Abstract

A novel composite column, consisting of an outer fiber reinforced polymer (FRP) tube, an engineered cementitious composite (ECC) ring and an inner high strength concrete (HSC) core, has been proposed and experimentally investigated in this study. Due to the high brittleness of HSC, localized cracks may occur and lead to premature failure for conventional FRP-confined HSC columns. With the excellent tensile and cracking behavior, ECC ring is used to redistribute the hoop stress and strain from HSC core to FRP tube in the proposed novel FRP-ECC-HSC composite column. A total of 12 stub columns with different HSC core strengths and ECC ring thicknesses were tested under axial compression. It is found that FRP-ECC-HSC composite columns can develop larger FRP confining efficiency with more uniform hoop strain distribution in comparison to the corresponding normal FRP-confined HSC columns. The ultimate axial strain is obviously enhanced as well for this composite column, leading to an improved ductile compressive behavior. Based on the test results obtained from this study, design equations are proposed to predict the ultimate loading capacity and ultimate axial strain for the FRP-ECC-HSC composite column.

Keywords: FRP-ECC-HSC, composite column, hoop strain distribution, load capacity, ultimate axial strain

1. Introduction

Fiber reinforced polymer (FRP) confined concrete is widely used in engineering applications, including strengthening and repair of old structures and construction of new structures [1-3]. With the effective confinement provided by FRP, concrete is under the state of triaxial stress and can exhibit significantly enhanced capacity and ductility performance under compressive loadings, compared with unconfined concrete [4-6]. High strength concrete (HSC) is showing the excellent advantages of increasing the structural bearing capacity, structural stiffness and reducing the self-weight. Similar to FRP-confined normal strength concrete (NSC), FRP-confined HSC can also achieve improved performance [7-10]. However, due to the increased brittleness of HSC, the compressive behavior for FRP-confined HSC columns is different from FRP-confined NSC columns [3,7,10-13]. Fig. 1 shows the typical failure modes for FRP-confined NSC and FRP-confined HSC stub columns under axial compression [14,15]. NSC crushes uniformly in the mid-height region of the column (Fig. 1(a)). Effective confinement is triggered with the uniform concrete dilation. On the contrary, HSC can develop localized shear crack from the top to the bottom, causing highly concentrated hoop strain and FRP rupture in the same cracking location (Fig. 1(b)). As reported in the literature, the average FRP rupture strain for FRP-confined HSC is lower than the corresponding FRP-confined NSC [16,17]. FRP-confining efficiency [18], which is determined by the ratio of average FRP rupture strain of the column over the FRP rupture strain obtained from material tests and generally in the range of 0.5-0.8 [2,19-22], would decrease with the increase of concrete strength [17,19]. This indicates that a relatively poorer confinement may be produced for FRP-confined HSC. The stress-strain relationship of FRP-confined HSC is also different from that of FRP-confined NSC. The stress normally drops after the first peak in the stress-strain curve, followed by a stress recovery if sufficient confinement can be provided later on for FRP-confined HSC [3,23,24]. For the ultimate conditions, enhancements of both compressive strength and ultimate axial strain are reduced for FRP-confined HSC [25,26]. Therefore, the weakened structural performance, especially the ductility behavior, causes a big challenge to the engineering application of FRP-confined HSC columns.

In this study, a novel FRP-ECC-HSC composite column is proposed to improve the compressive behavior of normal FRP-confined HSC column. The sectional arrangement is shown in Fig. 2. It has an FRP tube, an engineered cementitious composite (ECC) ring and a high strength concrete (HSC) core. ECC is a fiber reinforced cementitious composite with good ductility performance and can develop an ultimate tensile strain of 1% - 8% [27-30]. When a microcrack initiates in ECC, the fiber bridging the microcrack will prevent its width to continue increasing. Meanwhile, multiple microcracks will occur with the width in a stable state of less than 100 μm [29]. The main purpose of ECC ring in the composite column is to improve the hoop strain distribution behavior, which is closely related to the confinement behavior. The hoop strain distribution mechanisms are shown in Fig. 3 for FRP-confined HSC column and FRP-ECC-HSC composite column, respectively. When HSC core develops localized large cracks, ECC will generate multiple microcracks and help to redistribute the localized hoop strain from HSC core to FRP tube, leading to a much more uniform strain distribution on the

FRP tube. Therefore, the FRP premature rupture will be mitigated, leading to an improved FRP confining efficiency. The full utilization of FRP confining material will delay the column failure as well. Both compressive strength and deformability will be further enhanced accordingly. Meanwhile, the proposed FRP-ECC-HSC composite column is steel free, which indicates that it can be used in marine environments without the concern of steel corrosion problem.

The FRP-ECC-HSC composite column consists of two types of concrete under the confinement of FRP tube, which has not been investigated in the previous literature. This study focuses on the interaction behavior of the three components in the composite column, as well as the improved structural performance contributed by the ECC ring. Axial compression tests were carried out for both normal FRP-confined HSC columns and FRP-ECC-HSC composite columns. Failure modes, axial load-strain behavior, hoop strain behavior and ultimate conditions are presented and analysed in detail. Design equations have also been proposed to predict the ultimate loading capacity and ultimate axial strain for the FRP-ECC-HSC composite column based on the test results obtained from this study.

2. Experimental investigation

2.1 Material properties

2.1.1 HSC core

Two strengths of HSC, C70 and C90, were considered in this study. The mix proportions are given in Table 1. Compressive strengths were obtained from the compression tests on 150 mm × 300 mm cylinders, with the averaged results of 75.4 MPa for C70 and 96.8 MPa for C90. Elastic modulus and compressive strain at the peak stress were 32.0 GPa and 0.0028 for C70, and 35.3 GPa and 0.0032 for C90, respectively. Poisson's ratio was 0.21 for both C70 and C90.

2.1.2 ECC ring

ECC50 was used to form the ECC ring, with the mix proportions given in Table 2. The volume of polyethylene (PE) fiber of 2% was used in the ECC mixture. Fiber properties are provided in Table 3. Compressive strength was obtained from the compression tests on 75 mm × 150 mm cylinders, with the averaged result of 55.2 MPa. Elastic modulus and compressive strain at the peak stress were 15.3 GPa and 0.0046, respectively. Poisson's ratio was found to be 0.21.

Uniaxial tensile tests on ECC were carried out to obtain the tensile behavior following JCSE recommendation [31]. Specimen details and test setup are shown in Fig. 4. Typical multiple cracking behavior was observed for the ECC coupons under tension. Tensile stress-strain curves are presented in Fig. 5. Ductile strain hardening behavior can be observed for ECC50, with the tensile strength of 5.0 MPa and ultimate tensile strain of 3-4%.

2.1.3 FRP tube

Filament winding glass FRP tubes were used in this study. The tubes had 7 layers of fiber, with a nominal thickness of 2.5 mm. Fiber orientation was 80° along the longitudinal direction, to provide confinement on the infilled concrete. Tensile split-disk tests were carried out following ASTM D2290-08 [32] to obtain the hoop tensile behavior. 5 FRP rings, with the width of 50 mm, were cut from the FRP tubes and used as specimens for the tensile tests. Stress-strain curves are plotted in Fig. 6. Linear behavior was observed until the FRP rupture. The averaged ultimate tensile stress, ultimate tensile strain and elastic modulus for the FRP tubes in the hoop direction were 620.8 MPa, 0.0156 and 39.8 GPa, respectively.

Compression tests on 3 FRP rings, with the height of 60 mm, were carried out following the GB/T5350-2005 [33] to obtain the axial compressive behavior of the FRP tubes. Compressive stress-strain curves are plotted in Fig. 7. It can be observed that stress increases linearly at the initial stage, while nonlinear behavior with a significant stiffness decrease is noted later until buckling failure of the resin matrix occurs in the middle region of the FRP ring. Averaged ultimate compressive stress, ultimate compressive strain and elastic modulus at the initial linear stage were 70.6 MPa, 0.0106, and 9.5 GPa, respectively.

2.2 Test specimens

Eight specimens for FRP-ECC-HSC composite column were prepared and tested under monotonic axial compression. All of the specimens had the nominal diameter of 200 mm (inner diameter for FRP tube) and the nominal height of 400 mm. Two ECC ring thicknesses, 15 mm and 25 mm, as well as two grades of HSC were included. As for the specimen ID, F, E and H are representing the FRP, ECC and HSC, respectively. 15 or 25 stands for the ECC ring thickness. For example, "FE50H70-25" is the ID for the specimen with ECC50 as the 25 mm-thick ECC ring and C70 as HSC core (core diameter of 150 mm). Two identical specimens were prepared for FRP-ECC-HSC columns, with "R" referring to the repeated specimens.

Four FRP-confined HSC columns were prepared for comparison with the proposed FRP-ECC-HSC composite columns. Six specimens for ECC ring, ECC-confined HSC and FRP-confined ECC ring were also prepared and tested under axial compression. These specimens were also used for comparison purpose to better understand the comprehensive behavior of FRP-ECC-HSC composite columns. Details of all the specimens are summarized in Table 4.

Preparation procedures for FRP-ECC-HSC composite columns in laboratory are shown in Fig. 8(a). HSC core was firstly cast. After removing the mould, HSC core was then put in the centre of the FRP tube. Fixtures were used to guarantee the precise position. ECC was then poured into the gap between FRP tube and HSC core to form the ECC ring. Similar procedures were adopted for casting the other specimens of ECC ring, FRP-ECC and ECC-HSC, with the use of an inner or outer mould which would be demoulded after concrete hardening. The prepared specimens are shown in Fig. 9. In engineering practice, it is difficult to cast HSC core and ECC ring separately in construction site. ECC ring could be cast in factory like concrete pipes used in drainage engineering, followed by filament winding of FRP fibers on the outer surface to form the FRP-ECC tube as shown in Fig. 8(b). This prefabricated FRP-ECC tube can be transported to construction sites and used as formwork for HSC core casting directly, to form the FRP-ECC-HSC composite column. Shear connectors could also be arranged between the HSC core and ECC ring for the composite columns that may be subjected to potential eccentric compression in practice.

Three layers of CFRP, with the width of 20 mm, were wrapped near the two ends of all the specimens for strengthening, to avoid local failure during the compression tests. Capping with high strength gypsum material was adopted to flatten the top and bottom column surfaces and ensure the application of uniform pure compression during testing.

2.3 Test setup

Compression tests were carried out on the MTS 815 machine with a capacity of 4600 kN, as shown in Fig. 10(a). Displacement control with a loading rate of 0.24 mm/min was adopted. Fig. 10(b) shows the instrumentation of the specimen. Twelve strain gauges were installed in the mid-height of the column in the hoop direction at every 30° to measure the hoop strain distribution. Four strain gauges were installed in the mid-height of the column in the axial direction at every 90° for axial strain measurements. Two LVDTs were attached on the column surface, measuring the axial deformation of the 200 mm gauge length in the middle range of the column. Four LVDTs were put between the top and bottom loading plates, to measure the axial shortening of the column in the full height range. Axial compression load was applied on the concrete and FRP tube simultaneously. The load, strain gauge and LVDT readings were recorded by a data logger.

3. Experimental results

3.1 Test observations and failure modes

Typical failed specimens are shown in Fig. 11. All the specimens of FRP-confined HSC column and FRP-ECC-HSC composite column experienced similar behavior and failed by FRP rupture in the hoop direction (Figs. 11(a)-(c)). Before FRP rupture, local white rifts were observed, which indicated that resin failure occurred. With further axial shortening, FRP rupture occurred at one location and then propagated along the column.

For ECC ring specimens under compression, diagonal shear cracks were dispersed around the circumference (Fig. 11(d)). For FRP-confined ECC ring specimens, ECC would crush inwards due to the lack of inner support. Local buckling failure of FRP tube was also observed at the same location, while no FRP rupture occurred (Fig. 11(e)). For ECC-confined HSC specimens, inner HSC core failed firstly with a notable sound during the compression test. Then cracks initiated and propagated on the ECC ring mainly in the vertical direction (Fig. 11(f)). ECC would provide confinement on the crushed HSC core, keeping the whole specimen intact.

3.2 Axial load-axial strain curves

In the tests, axial strains were measured by axial strain gauges, and can also be calculated by the readings from full height and mid height LVDTs. Fig. 12 presents the axial load-axial strain curves for specimen FE50H90-15, in which the axial strains were determined by strain gauges, full height LVDTs and mid height LVDTs, respectively. It can be noted that the results obtained by the three approaches are nearly coincident with each other before reaching the first peak load. After the first peak, the difference becomes greater with the increase of axial shortening. This is due to that the concrete cracks after the first peak, forming significant localized deformation and damage in concrete and slips between concrete and FRP tube. Meanwhile, strain gauges and mid height LVDTs would fail and could not last to the end of the test when resin failure or FRP rupture just occurred at the corresponding locations, since they were directly attached to the FRP tube surface. This behavior has also been noted by previous studies on concrete filled FRP tube and is especially obvious for HSC with high brittleness [34]. It is believed that the readings obtained by the full height LVDTs are more reliable to reflect the general axial strain behavior of the composite column. Therefore, axial strain calculated by the average reading of the four full height LVDTs was used for analysis in this study. Full heights of all the columns were measured carefully before the tests to ensure the accurate conversion from axial shortenings to axial strains.

Axial load-axial strain curves for FRP-confined HSC and FRP-ECC-HSC specimens are presented in Figs. 13(a)-(f). All the curves show a typical three-stage behavior. There is a strain softening stage after the first peak, followed by stress recovery until FRP rupture. It can be observed from the curves that FRP-ECC-HSC specimens have less load drops after the first peak and develop more stable ascending linear branches for the strain hardening stage, compared with the corresponding FRP-confined HSC specimens.

Figs. 13(g)-(i) show the axial load-axial strain responses of hollow ECC ring, FRP-confined ECC ring and ECC-confined HSC specimens under axial compression. Sudden load drop occurs after the peak, with a relatively low residual capacity remained for ECC ring specimens (Fig. 13(g)). This behavior is also evident from the research on ECC material under compression [35,36]. FRP-confined ECC ring specimens will develop a relatively smaller load drop after the peak, then followed by a stress recovery due to the confinement effect by the FRP tube (Fig. 13(h)). Compared with hollow ECC ring specimens, FRP-confined ECC ring specimens have a much larger residual capacity and stable descending stage for the post-peak behavior, leading to better ductility performance under axial compression. For ECC-confined HSC specimens, there is a significant load loss when the inner HSC core crushes (Fig. 13(i)). The maximum load for ECC-HSC is relatively higher than the sum of the load of HSC core and ECC ring at the corresponding axial strain. Meanwhile, the axial strain at the peak load of the ECC-HSC specimen is relatively larger than the axial strain at the peak strength of the plain HSC. It indicates that both compressive strength and strain can be enhanced for HSC under the confinement of ECC ring to some extent.

Major characteristics for all the tested specimens are summarized in Table 5 to further quantify the axial compressive behavior. F_1 and F_2 are the first peak load and the load corresponding to the initial point of the stress recovery branch, respectively; F_c and ε_{cc} are the ultimate load and ultimate axial strain at FRP rupture. For FRP-confined ECC ring specimens, F_c and ε_{cc} refer to the load and axial strain corresponding to the last point of the strain hardening stage. $\varepsilon_{h,rup}$ is the average hoop strain at FRP rupture.

4. Analysis and discussions

4.1 Typical compressive behavior

The interactions among axial stress, axial strain and lateral strain for FRP-confined HSC are illustrated in detail in Fig. 14. In the initial stage OA, hoop strain increases slowly and the increasing slope can be regarded as the same as the Poisson's ratio of concrete. After the first peak, HSC core cracks or even crushes due to its high brittleness. There is a load drop in this strain softening stage AB, accompanied by the rapid increase of hoop strain. Confining pressure is large enough to provide effective confinement on inner concrete when reaching point B. Axial compressive stress starts to recover stably in the strain hardening stage BC, until reaching the FRP rupture strain $\varepsilon_{h,rup}$ at Point C.

Fig. 15 presents the comparison of the load-strain response before FRP rupture between FRP-confined HSC and FRP-ECC-HSC specimens. Axial load-axial strain curves are plotted on the right side, while axial load-hoop strain curves are plotted on the left side of the graphs. The hoop strains were calculated by averaging the readings of 12 hoop strain gauges. In the initial stage, FRP-ECC-HSC specimens have relatively lower stiffness than FRP-confined HSC specimens, which is caused by the lower elastic modulus of ECC. Similarly, the first peak load F_1 becomes lower with the increase of ECC thickness from 0 to 25 mm. Compared with FRP-confined HSC specimens, the load drop is less obvious and the strain softening stage is shorter for FRP-ECC-HSC specimens. The ratio of F_2/F_1, as listed in Table 5, are larger and closer to one for FRP-ECC-HSC specimens in comparison to FRP-confined HSC specimens. For ultimate conditions, compressive strain is increased with the increase of ECC proportion, indicating the FRP-ECC-HSC specimens can develop larger deformability under axial compression. The ultimate load capacities are similar for FRP-ECC-HSC and FRP-confined HSC specimens with C70 as HSC core. For specimens with C90 as HSC core, however, the ultimate load capacity of the FRP-ECC-HSC composite column is relatively lower, due to the larger difference of the compressive strength between ECC50 and C90.

4.2 Hoop strains

Hoop strain is a key characteristic investigated in this study. It reflects the dilation behavior of confined concrete as well as the confinement level provided by FRP tube. To observe the dilation and cracking behavior of inner HSC and ECC, FRP tubes were removed after tests. Typical cracking pattens for FRP-confined HSC and FRP-ECC-HSC specimens are shown in

Fig. 16. Hoop strain distributions for the corresponding specimens, which were based on the readings of the hoop strain gauges installed on the FRP tube, are also plotted in Fig. 16 for comparison with the cracking pattens. For FRP-confined HSC specimens (Fig. 16(a)), localized diagonal crack separated the HSC core into two parts. It is also evident from the outstanding strain value at location 5 (h5) in the hoop strain plot. For FRP-ECC-HSC specimens, on the contrary, uniform cracks developed around the column (Figs. 16(b)-(c)), accompanied by a uniform hoop strain distribution. With the ECC ring thickness increased from 15 mm to 25 mm, cracks on the ECC surface became finer, leading the hoop strain distribution to be uniform further. When ECC ring was peeled off for FRP-ECC-HSC specimens, HSC core crushing was observed inside as shown in Fig. 17. It indicates that ECC ring is effective to redistribute and even the hoop strain from HSC core to FRP tube, which also confirms the mechanism proposed for the novel FRP-ECC-HSC composite column as presented in Fig. 3. With this more uniform hoop strain distribution, average hoop strains at FRP rupture $\varepsilon_{h,rup}$ are also increased for FRP-ECC-HSC specimens compared with the corresponding FRP-confined HSC specimens, as listed in Table 5.

FRP confining efficiency k_{ε}, which is calculated by the ratio of averaged hoop rupture strain $\varepsilon_{h,rup}$ over the rupture strain obtained from material tests, is summarized in Table 5 and plotted in Fig. 18. On average, with the contribution of ECC ring, k_{ε} is increased by 3-19% and 7-14% for C70 and C90 series, respectively. The improved k_{ε} value demonstrates that FRP-ECC-HSC columns could develop larger FRP confining efficiency than the corresponding FRP-confined HSC columns under axial compression. It also indicates that the confining FRP material could be more fully utilized with ECC ring added in the composite columns.

Typical hoop strain-axial strain curves for FRP-ECC-HSC composite columns under axial compression are plotted in Fig. 19. Similar behavior can be observed when compared with FRP-confined HSC specimens. With the increase of ECC thickness from 0 to 25 mm, the hoop strain increases more slowly and presents a relatively lower value under the same axial strain. This difference is believed to be caused by the self-confinement effect of ECC. Dilation of ECC could be restrained with the fibers bridging through the cracks. It is also observed in the existing literatures that the hoop strain shows a slower development with the increase of axial strain for confined ECC cylinders compared with that for confined normal concrete cylinders under the same confinement level [37-39]. Equations for predicting the hoop strain-axial strain relationships proposed for FRP-confined normal concrete [11,12,17] could be no longer applicable to FRP-confined ECC. This behavior can also lead to that the hoop strain of the HSC core is relatively larger than that of the FRP tube in the FRP-ECC-HSC composite columns, and the difference will increase with the increase of ECC thickness. Last points of the hoop strain-axial strain curves as shown in Fig. 19 are associated with FRP rupture. Since the confining efficiency is increased for FRP-ECC-HSC specimens, the hoop strain at FRP rupture is increased accordingly. Axial strain at FRP rupture, which is also termed as the ultimate axial strain, is also enhanced significantly for FRP-ECC-HSC specimens due to the following two reasons: (1) the FRP rupture strain, which governs the column failure, is improved; (2) the slope of the hoop strain-axial strain curve is lower, resulting in a larger axial strain when reaching the certain hoop rupture strain.

4.3 Load capacity and ultimate axial strain

In this study, all the specimens confined with FRP tube have a strain softening stage after the first peak, then followed by the stress recovery until reaching the ultimate axial load and axial strain at FRP rupture. As presented in Table 5, the ultimate load F_c is nearly the same or even lower compared with the first peak load F_1 for FRP-confined HSC specimens. However, F_c is always larger than F_1 for the tested FRP-ECC-HSC specimens, indicating an effective confinement achieved in terms of loading capacity. Load capacity enhancement ratio defined as F_c/F_1 is also calculated and listed in Table 5. It can be seen that F_c/F_1 is increased with the increase of ECC proportion. The comparison of ultimate load capacity at FRP rupture for the tested specimens is plotted in Fig. 20(a). It shows that relatively close loading capacity can be achieved after adding an ECC layer in the composite column for the specimens with C70 as HSC core, while the loading capacity decreases with the increase of ECC thickness for the specimens with C90 as HSC core.

Ultimate axial strain at FRP rupture is a key parameter investigated in this study. A larger ultimate axial strain reflects a better axial shortening behavior for FRP-confined concrete columns under axial compression, which also means a better ductility performance. Ultimate axial strains ε_{cc} of the tested specimens are presented in Table 5 and Fig. 20(b), which are effectively improved for the FRP-ECC-HSC specimens in comparison to the corresponding FRP-confined HSC specimens. On average, ultimate axial strain is increased by 5% and 33% for FE50H70-15 and FE50H70-25, as well as 9% and 20% for FE50H90-15 and FE50H90-25. Meanwhile, it is also observed that the ultimate axial strain decreases with the increase of HSC strength from C70 to C90, for both FRP-confined HSC specimens and FRP-ECC-HSC specimens.

5. Prediction of ultimate conditions

5.1 Load capacity

In FRP-ECC-HSC composite column, the three components, HSC core, ECC ring and FRP tube, are loaded simultaneously under axial compression. The ultimate load capacity at FRP rupture can be calculated through the superposition of the axial loads carried by different components. Therefore, the following equation is proposed to predict the ultimate load of the FRP-ECC-HSC composite column:

$$F = A_{hsc}f_{hsc} + A_{ecc}f_{ecc} + A_{frp}f_{frp} \quad (1)$$

where A_{hsc}, A_{ecc} and A_{frp} are the cross-sectional areas of HSC core, ECC ring and FRP tube, respectively; f_{hsc}, f_{ecc} and f_{frp} are the compressive stresses of HSC core, ECC ring and FRP tube at FRP rupture, respectively.

It is noted that the FRP tube could also contribute to axial load carrying capacity in the composite column, though the compressive strength and elastic modulus in the axial direction are obviously lower than the tensile strength and elastic modulus in the hoop direction due to the fiber orientation. The axial strains at FRP rupture for all the specimens were larger than the ultimate compressive strain of FRP tube, which was 0.0106 obtained by material tests. Therefore, f_{frp} is assumed to be equal to the ultimate compressive stress of FRP tube, which is 70.6 MPa. Even though FRP tube may occur the resin failure in the axial direction before rupture in the hoop direction, the capacity is believed not to lose immediately with the support of inner concrete. Meanwhile, the load capacity contributed by FRP tube is significantly lower than that contributed by the inner confined concrete, indicating that less difference will be caused by this assumption.

With the different compressive properties between HSC core and ECC ring in the composite column, the stress distribution on the column section is different from the FRP-confined solid concrete column. For the HSC core with solid circular section, it is under uniform confinement. For the ECC ring with annular section, it is under non-uniform confinement. The tensile strength of ECC is much lower than that of the FRP tube. Meanwhile, ECC is under triaxial compression in the composite column with the confinement provided by the outer FRP tube. Therefore, there is no hoop tensile stress component in the ECC ring, which means that the

ECC ring cannot provide additional confinement to the HSC core. The confinement effect applied on the HSC core is provided by the FRP tube only. Confining pressure f_l is directly related to the lateral strain and can be calculated as follows:

$$f_l = K_l \varepsilon_l = \frac{2E_{frp}\varepsilon_l t_{frp}}{D} \tag{2}$$

where E_{frp} and t_{frp} are elastic modulus and thickness of the confining FRP tube; K_l is confining stiffness; ε_l is lateral strain (hoop strain) and D is the inner diameter of FRP tube.

Extensive design models with closed forms have been proposed in the literature [9,40-42] to predict the ultimate compressive strength of FRP-confined concrete. Lim and Ozbakkaloglu [40] proposed a design model to predict the ultimate conditions after incorporating a large test database of FRP-confined high strength concrete. The model is able to consider the situation of medium confinement, in which there is a strain softening stage after the first peak load, then followed by stress recovery until FRP rupture as shown in Fig. 14. As reported, all the specimens present this behavior in this study. Therefore, Lim and Ozbakkaloglu's model [40] is adopted here to predict the compressive stress of HSC core f_{hsc}. It is expressed as follows:

$$f_{hsc} = af'_{c0} + 2.81(f_{lu} - f_{l0}) \tag{3}$$

$$f_{lu} = K_l \varepsilon_{h,rup} \tag{4}$$

$$f_{l0} = bK_l \varepsilon_{c0} \tag{5}$$

in which f'_{c0} and ε_{c0} are unconfined HSC strength and the corresponding compressive strain; $\varepsilon_{h,rup}$ is hoop strain at FRP rupture. f_{lu} and f_{l0} are the actual confining pressures at FRP rupture (point C in Fig. 14) and at the initial point of the stress recovery branch (point B in Fig. 14). It is noted that the parameters a and b can be determined by empirical equations, which are associated with concrete strength and confining stiffness as suggested by Lim and Ozbakkaloglu [40]. In this current study, however, a and b are assigned with the values of 1 and 2.8 for C70, as well as 0.9 and 2.4 for C90 to best fit the test results of FRP-confined HSC specimens. Eq. (3) considers the strength enhancement effect according to the equivalent confining pressure $f_{lu} - f_{l0}$, which is subtracting the confining pressure f_{l0} at the initial point of the stress recovery branch from the actual confining pressure f_{lu} at FRP rupture. Therefore, the coefficient 2.81 could be understood as the strength enhancement coefficient for this stress recovery branch of FRP-confined HSC.

ECC ring was subjected to non-uniform confinement in the composite column, because of the different properties between HSC core and ECC ring. Two principal stresses in the lateral direction are not equal to each other and they both vary with the changing of different locations. For simplification, a reduction factor of confining pressure k is adopted here to consider this effect. The equivalent confining pressure applied on ECC ring $f_{lu,ring}$ can be expressed as:

$$f_{lu,ring} = kf_{lu} \tag{6}$$

Dang et al. [37] conducted axial compression tests on FRP-confined ECC and proposed a design equation for ultimate compressive strength prediction, which is expressed as:

$$f_{ecc} = f'_{c0,ecc} + 2.5f_{lu,ring} \tag{7}$$

where $f'_{c0,ecc}$ is unconfined ECC strength. Eqs. (2)-(7) are adopted in Eq. (1) to predict the ultimate loading capacity of FRP-ECC-HSC specimens. It is found that $k = 0.7$ best fits the test results. Comparisons between test results and predictions are presented in Table 6 and Fig. 21(a). It can be seen that the proposed equation can provide close predictions on the ultimate load capacity of the FRP-ECC-HSC composite column, with the mean value of 0.98 and coefficient of variation (CoV) value of 0.044. The predictions for all the test data are within the ±10% error, which also indicates the reliability of the proposed equations. It is worth noting that relatively larger predicted results were obtained for the specimens with ECC thickness of 25 mm as presented in Table 6, which is believed to be caused by the adopted Dang et al.'s design equation [37] for FRP-confined ECC with the strength enhancement coefficient of 2.5 as shown in Eq. (7). In the literature, both the experimental investigations and design models of FRP-confined ECC are relatively limited. Dang et al. [37] proposed the coefficient of 2.5 based on their own test data. More accurate prediction equations on the compressive strength of FRP-confined ECC can also be developed with more available test data in future studies, and then adopted in the prediction model for ultimate load capacity of the FRP-ECC-HSC composite columns.

5.2 Ultimate axial strain

Most of the existing expressions for the prediction of ultimate axial strain of FRP-confined concrete adopt the function of confining pressure corresponding to the FRP rupture. Similar to compressive strength, Lim and Ozbakkaloglu's model [40] provides reasonable predictions on ultimate axial strain of FRP-confined HSC. The following expression, which is modified from Lim and Ozbakkaloglu's model [40], is adopted in this study:

$$\varepsilon_{cc} = c\varepsilon_0 + 0.303(\frac{K_l}{f'_{co,ave}})\varepsilon_{h,rup}^{1.35} \quad (8)$$

$$f'_{co,ave} = (f'_{c0,hsc}A_{hsc} + f'_{c0,ecc}A_{ecc})/(A_{hsc} + A_{ecc}) \quad (9)$$

where $f'_{c0,hsc}$, $f'_{c0,ecc}$ and $f'_{c0,ave}$ are the unconfined strength of HSC core, unconfined strength of ECC ring and averaged unconfined strength of HSC core and ECC ring. Factor c is related with concrete strength as suggested by Lim and Ozbakkaloglu [40]. In this study, c is assigned to be 1.7 and 1.4 for specimens with C70 and C90 as HSC core respectively, to best fit the test results. For the prediction of FRP-ECC-HSC specimens, ε_0 of the corresponding HSC core is adopted, though the compressive strain at peak strength of ECC is larger than that of the HSC. The benefit of ultimate axial strain for FRP-ECC-HSC over FRP-HSC is considered by the enhanced FRP rupture strain $\varepsilon_{h,rup}$. Comparisons between test results and predictions are presented in Table 6 and Fig. 21(b). It is shown that the predictions given by Eqs. (8-9) agree well with the test results, with the mean value of 1.00 and CoV value of 0.039.

It is noted that parameters a and b in Eq. (3) and c in Eq. (8) determined by the test data in this current study may be different from those given in the literature [40], which are determined by a large database including different concrete strengths and confinement levels. Since only C70 and C90 HSC core are included in this current study, parameters given by the literature are not best fitting the test results. Therefore, the modified parameters are used herein. Meanwhile, as suggested in the literatures [23,43], the presented ultimate conditions at FRP rupture can be used with other key points, including the first peak point and the transition point between the strain softening and strain hardening stages, to determine the design-oriented stress-strain curve for FRP-confined concrete. Therefore, the overall load-strain curve can then be generated through the superposition of the axial loads carried by the different components for the FRP-ECC-HSC composite columns.

Actual FRP rupture strain $\varepsilon_{h,rup}$ of each specimen is used in the predictions presented above. It shows that the models adopted for both ultimate load capacity and ultimate axial strain can provide accurate predictions, if the accurate FRP rupture strain is used. In this current stage of the preliminary investigation on the FRP-ECC-HSC specimens, expression on the prediction of FRP rupture strain $\varepsilon_{h,rup}$ is not given due to the limited test data. In the next step, the prediction models on the FRP rupture strain for FRP-ECC-HSC composite columns need to be developed with the help of a larger test database.

6. Conclusions

A novel FRP-ECC-HSC composite column was proposed and experimentally investigated under monotonic axial compression in this study. Failure modes, axial load-axial strain and hoop strain-axial strain responses were presented. Design equations on the ultimate conditions of the composite column were proposed. Within the current scope of this study, the following conclusions can be drawn:

(1) FRP-ECC-HSC composite columns can develop more uniform hoop strain distribution in comparison to the corresponding normal FRP-confined HSC columns. It demonstrates that the ECC can redistribute the hoop strain from locally cracked HSC core to the outer FRP tube.

(2) With the increase of ECC proportion, the hoop strain distribution becomes more uniform. It is also found that the hoop strain develops relatively slowly with the increase of axial strain for FRP-ECC-HSC composite columns, indicating the ECC ring has the effect of restraining lateral dilation.

(3) The uniform hoop strain distribution leads to a larger average FRP rupture strain. FRP confining efficiency was increased by 3-19% and 7-14% for C70 and C90 series, respectively. The failure of FRP-ECC-HSC composite columns was consequently delayed.

(4) Compared with FRP-confined HSC columns, FRP-ECC-HSC composite columns exhibited less load drop after the first peak in the axial load-strain curve. The transition period from the initial stage to the strain hardening stage became shorter with the increase of ECC thickness.

(5) Compared with FRP-confined HSC columns, FRP-ECC-HSC composite columns can develop a similar ultimate loading capacity for specimens with C70 as HSC core, while a relatively lower ultimate loading capacity for specimens with C90 as HSC core. The ultimate load is enhanced compared with the load corresponding to the first peak point for all FRP-ECC-HSC specimens, exhibiting an effective confinement.

(6) The ultimate axial strain of FRP-ECC-HSC composite columns is obviously improved in comparison to FRP-confined HSC columns, showing a larger deformability and better ductility performance. The enhancement ratio is 5-33% and 9-20% for C70 and C90 series, respectively, and increases with the increase of ECC proportion.

(7) The proposed equations consider the appropriate compressive strength and strain of HSC core and ECC ring under FRP confinement and can give close predictions on the

ultimate load capacity as well as the ultimate axial strain of the FRP-ECC-HSC composite columns.

For the FRP tube, the glass fiber orientation is 80 degrees to the longitudinal direction in this current study, which is close to the circumferential direction to provide confinement to the inner concrete. With the increase of fiber angle with respect to the longitudinal direction, the higher confinement effect can be achieved accordingly. Meanwhile, the confinement effect will increase with the increase of modulus of elasticity and ultimate hoop tensile strain of the FRP tube. For the ECC ring, the strength is related to the loading capacity of the composite column, while the modulus of elasticity and compressive strain are related to the loading stage before the first peak point in the axial load-strain curve. With the increase of the elastic modulus and compressive strain of ECC, the initial stiffness and the axial strain corresponding to the first peak point will increase, respectively. It is worth noting that the compressive strength of ECC is lower than that of the HSC in this current study. ECC mixture with higher compressive strength can be explored in future studies, to achieve the further improved load carrying capacity, as well as maintain the good deformability and ductility performance for the FRP-ECC-HSC composite column.

CRediT authorship contribution statement

Shuai Li: Investigation, Writing - original draft. **Tak-Ming Chan:** Writing - review & editing, Funding acquisition, supervision. **Ben Young:** Writing - review & editing, Funding acquisition, Supervision.

Declaration of Competing Interest

The authors declare that they have no known competing financial interests or personal relationships that could have appeared to influence the work reported in this paper.

Acknowledgement

The research work presented in this paper was supported by the Research Grants Council of the Hong Kong Special Administrative Region, China – Theme-based Research Scheme (Project No. T22-502/18-R).

References

[1] Lam L, Huang L, Xie JH, Chen JF. Compressive behavior of ultra-high performance concrete confined with FRP. Compos Struct 2021;274:114321.

[2] Lam L, Teng JG. Ultimate condition of fiber reinforced polymer-confined concrete. J Compos Constr 2004;8(6):539–48.

[3] Ozbakkaloglu T. Behavior of square and rectangular ultra high strength concrete-filled FRP tubes under axial compression. Compos Part B 2013;54:97–111.

[4] Lam L, Teng JG. Design-oriented stress-strain model for FRP-confined concrete. Constr Build Mater 2003;17(6):471–89.

[5] Shayanfar J, Barros JAO, Rezazadeh M. Generalized Analysis-oriented model of FRP confined concrete circular columns. Compos Struct 2021;270:114026.

[6] Yang JQ, Feng P. Analysis-oriented model for FRP confined high-strength concrete: 3D interpretation of path dependency. Compos Struct 2021;278:114695.

[7] Ozbakkaloglu T, Vincent T. Axial compressive behavior of circular high-strength concrete-filled FRP tubes. J Compos Constr 2014;18(2):04013037.

[8] Lim JC, Ozbakkaloglu T. Stress-strain model for normal and light-weight concretes under uniaxial and triaxial compression. Constr Build Mater 2014;71:492–509.

[9] Ozbakkaloglu T, Lim JC, Vincent T. FRP-confined concrete in circular sections: Review and assessment of stress–strain models. Eng. Struct 2013;49:1068–1088.

[10] Wang WQ, Wu CQ, Liu ZX, Si HL. Compressive behavior of ultra-high performance fiber-reinforced concrete (UHPFRC) confined with FRP. Compos Struct 2018;204:419–37.

[11] Jiang T, Teng JG. Analysis-oriented stress-strain models for FRP-confined concrete. Eng. Struct 2007;29:2968-2986.

[12] Teng JG, Huang Y, Lam L, Ye L. Theoretical model for fiber-reinforced polymer confined concrete. J Compos Constr 2007;11(2):201–10.

[13] Lim JC, Ozbakkaloglu T. Unified stress-strain model for FRP and actively confined normal-strength and high-strength concrete. J Compos Constr 2015;19(4):04014072.

[14] Jiang C, Wu YF, Jiang JF. Effect of aggregate size on stress-strain behavior of concrete confined by fiber composites. Compos Struct 2017;168:851-862.

[15] Sirach N, Smith ST, Yu T, Mostafa A. Experimental study on the confinement of concrete cylinders with large rupture-strain FRP composites. J Compos Constr 2021;25(4):04021026.

[16] Wu YF, Jiang JF. Effective strain of FRP for confined circular concrete columns. Compos Struct 2013;95:479-491.

[17] Lim JC, Ozbakkaloglu T. Hoop strains in FRP-confined concrete columns: Experimental investigations. Mater Struct 2014;48(9):2839-2854.

[18] Pessiki S, Harries KA, Kestner JT, Sause R, Ricles JM. Axial behavior of reinforced concrete columns confined with FRP jackets. J Compos Constr 2001;5(4):237-245.

[19] Ozbakkaloglu T, Lim JC. Axial compressive behavior of FRP-confined concrete: Experimental test database and a new design-oriented model, Compos Part B 2013;55:607–634.

[20] Kashi A, Ramezanianpour AA, Moodi F, Malekitabar H. Effect of aggressive marine environment on strain efficiency factor of FRP-confined concrete. Constr Build Mater 2019;222:882-891.

[21] Lim JC, Ozbakkaloglu T. Influence of silica fume on stress–strain behavior of FRP-confined HSC. Constr Build Mater 2014;63:11-24.

[22] Smith ST, Kim SJ, Zhang H. Behavior and effectiveness of FRP wrap in the confinement of large concrete cylinders. J Compos Constr 2010;14(5):573-582.

[23] De Oliveira DS, Raiz V, Carrazedo R. Experimental study on normal-strength, high-strength and ultrahigh-strength concrete confined by carbon and glass FRP laminates. J Compos Constr 2019;23(1):04018072.

[24] Ozbakkaloglu T. Compressive behavior of concrete-filled FRP tube columns: Assessment of critical column parameters. Eng. Struct 2013;51:188-199.

[25] Pour AF, Ozbakkaloglu T, Vincent T. Axial compressive behavior of ultra-high-strength steel fiber-reinforced concrete-filled fiber reinforced polymer (FRP) tube columns. Compos Struct 2021;266:113777.

[26] Keshtegar B, Gholampour A, Thai DK, Taylan O, Trung NT. Hybrid regression and machine learning model for predicting ultimate condition of FRP-confined concrete. Compos Struct 2021;262:113644.

[27] Li VC, Wang S, Wu C. Tensile strain-hardening behavior of polyvinyl alcohol engineered cementitious composite (PVA-ECC). ACI Mater J 2001;98(6):483–92.

[28] Huang BT, Wu JQ, Yu J, Dai JG, Keung, CKY. High-Strength Seawater Sea-sand Engineered Cementitious Composites (SS-ECC): Mechanical Performance and Probabilistic Modeling. Cem Concr Compos 2020;114:103740.

[29] Li VC. On engineered cementitious composites (ECC). J Adv Concr Technol 2003;1(3):215–30.

[30] Ding Y, Yu J-T, Yu K-Q, Xu S-L. Basic mechanical properties of ultra-high ductility cementitious composites: From 40 MPa to 120 MPa. Compos Struct 2018;185:634–45.

[31] Japan Society of Civil Engineers. Recommendations for design and construction of high performance fiber reinforced cement composites with multiple fine cracks (HPFRCC). Concrete Engineering Series 82, 2008.

[32] ASTM D2290-08. Standard Test Method for Apparent Hoop Tensile Strength of Plastic or Reinforced Plastic Pipe by Split Disk Method, American Society for Testing and Materials, Philadelphia, USA, 2008.

[33] GB/T5350-2005. Fiber-Reinforced Thermosetting Plastic Composites Pipe: Determination for Longitudinal Compressive Properties, The Standards Press of China, 2005.

[34] Zhang B, Yu T, Teng JG. Behavior of concrete-filled concrete tubes under cyclic axial compression. J Compos Constr 2015;19(3):04014060.

[35] Zhou JJ, Pan JL, Leung CKY. Mechanical behavior of fiber reinforced engineered cementitious composites in uniaxial compression. J Mater Civ Eng 2015;27(1):04014111.

[36] Meng D, Huang T, Zhang YX, Lee CK. Mechanical behaviour of a polyvinyl alcohol fibre reinforced engineered cementitious composite (PVA-ECC) using local ingredients. Constr Build Mater 2017;141:259-270.

[37] Dang Z, Feng P, Yang JQ, Zhang Q. Axial compressive behavior of engineered cementitious composite confined by fiber-reinforced polymer. Compos Struct 2020;243:112191.

[38] Yuan WY, Han Q, Bai YL, Du XL, Yan ZW. Compressive behavior and modelling of engineered cementitious composite (ECC) confined with LRS FRP and conventional FRP. Compos Struct 2021;272:114200.

[39] Li Y, Wang W, Wen C. Experiment study on mechanical performance of ECC under conventional triaxial compression. Concrete 2016;1:59–63.

[40] Lim JC, Ozbakkaloglu T. Confinement model for FRP-confined high strength concrete. J Compos Constr 2014;18(4):4013058.

[41] Jiang K, Han Q, Bai YL, Du XL. Data-driven ultimate conditions prediction and stress-strain model for FRP-confined concrete. Compos Struct 2020;242:112094.

[42] Isleem HF, Feng P, Tayeh BA. Confinement model for LRS FRP-confined concrete using conventional regression and artificial neural network techniques. Compos Struct 2021;279:114779.

[43] Liao J, Zeng JJ, Gong QM, Quach WM, Gao WY, Zhang L. Design-oriented stress-strain model for FRP-confined ultra-high performance concrete (UHPC). Constr Build Mater 2022;318:126200.

(a) NSC (f'_{c0} =28.38 MPa) [14] (b) HSC (f'_{c0} =110 MPa) [15]

Fig.1 Typical failure modes for FRP-confined concrete

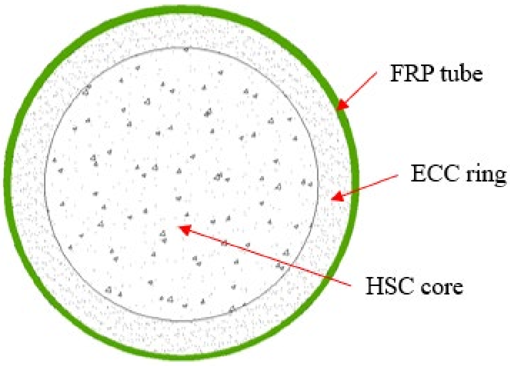

Fig. 2 Section of FRP-ECC-HSC composite column

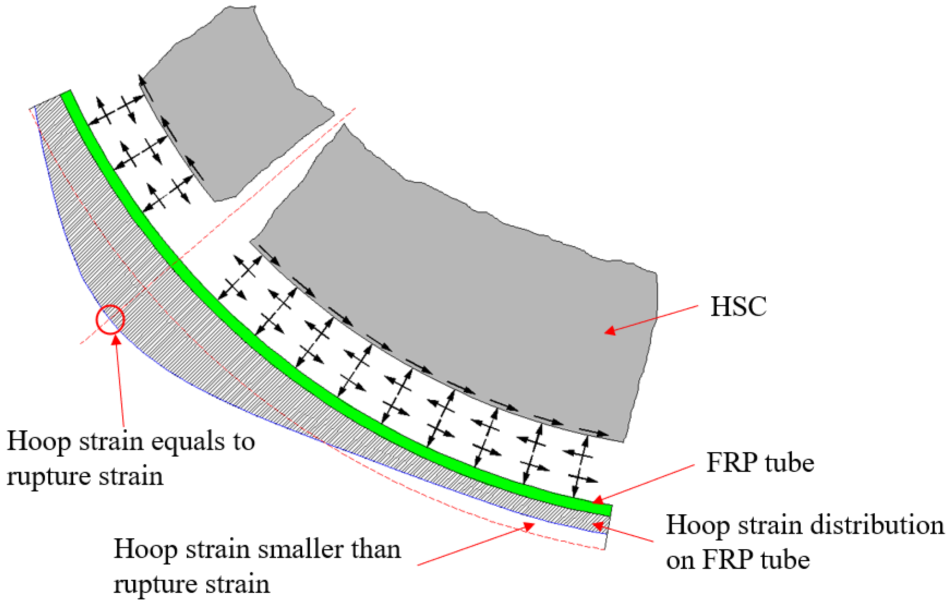

(a) FRP-confined HSC column

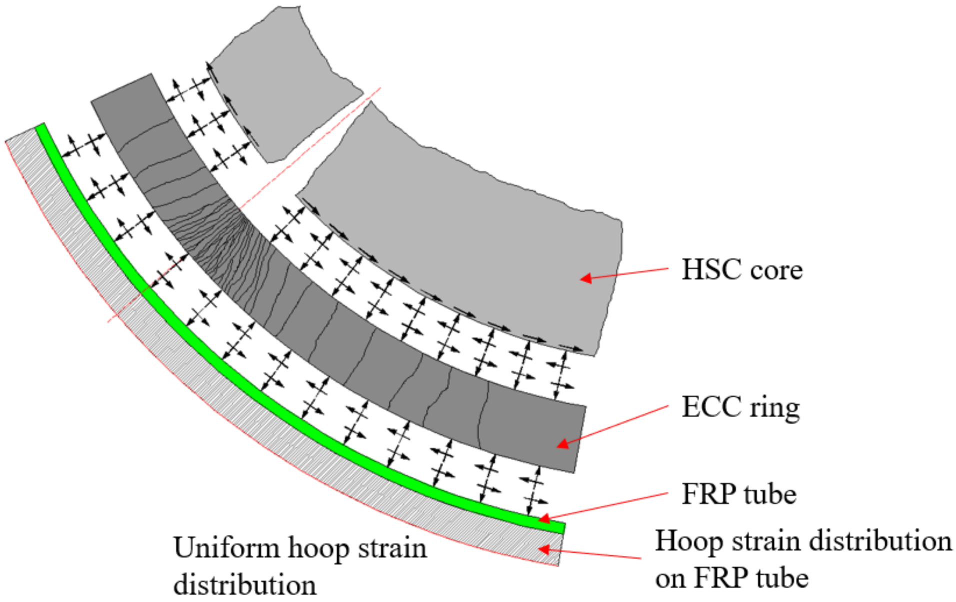

(b) FRP-ECC-HSC composite column

Fig. 3 Hoop strain distribution mechanisms for FRP-confined concrete columns

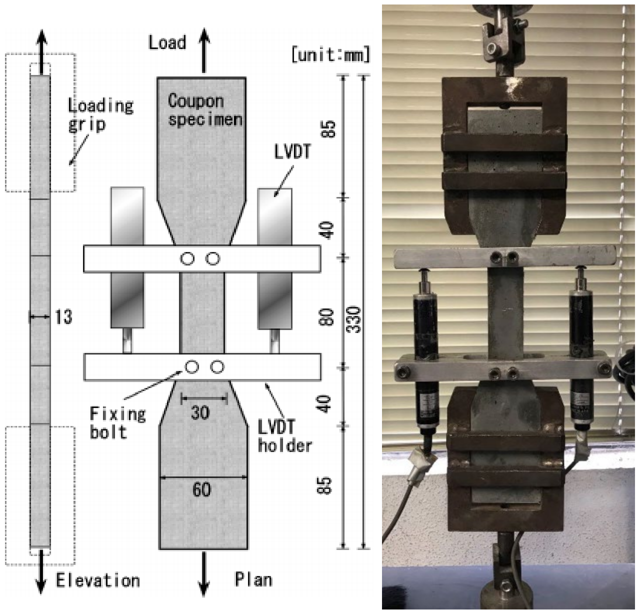

Fig. 4 Details of tensile coupon (JSCE [31]) and test setup

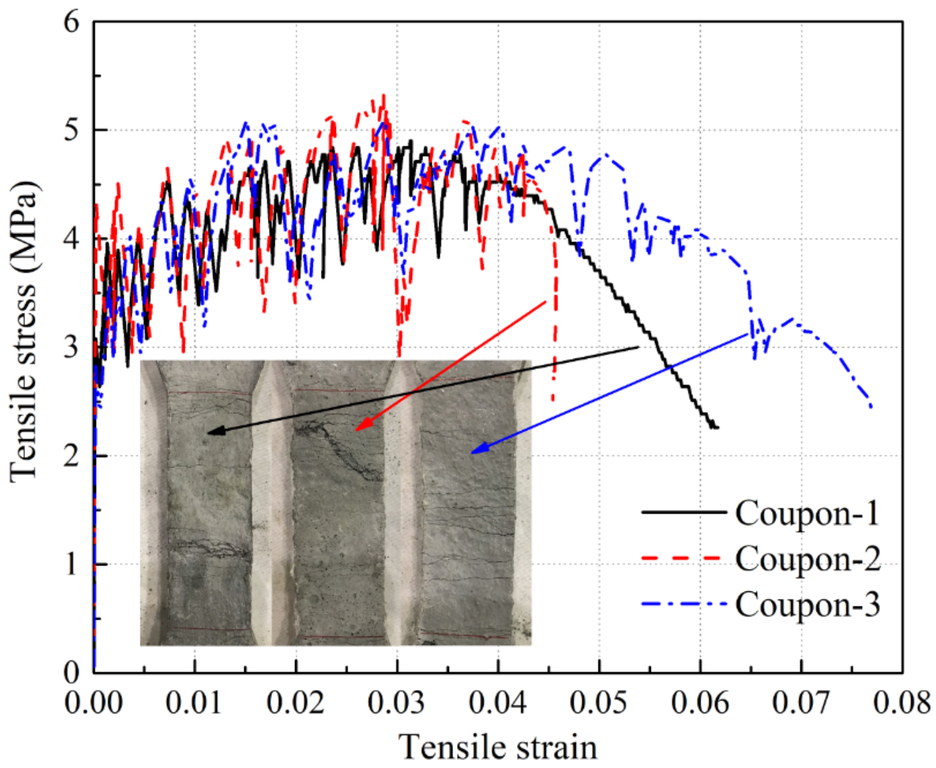

Fig. 5 Tensile stress-strain curves of ECC coupons

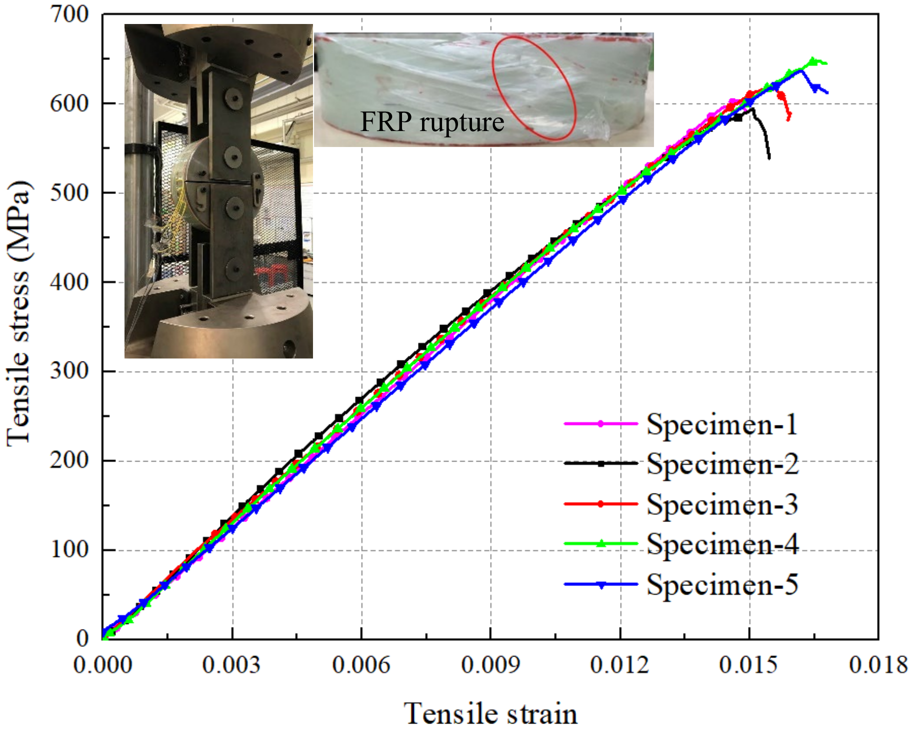

Fig. 6 Stress-strain curves for tensile split-disk tests

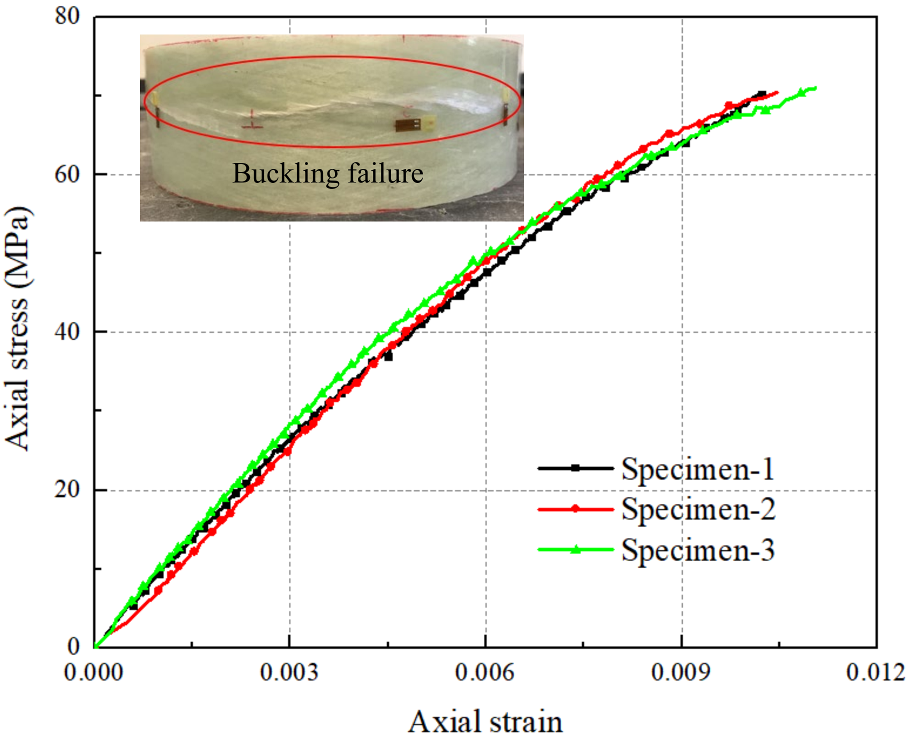

Fig. 7 Stress-strain curves for ring compression tests

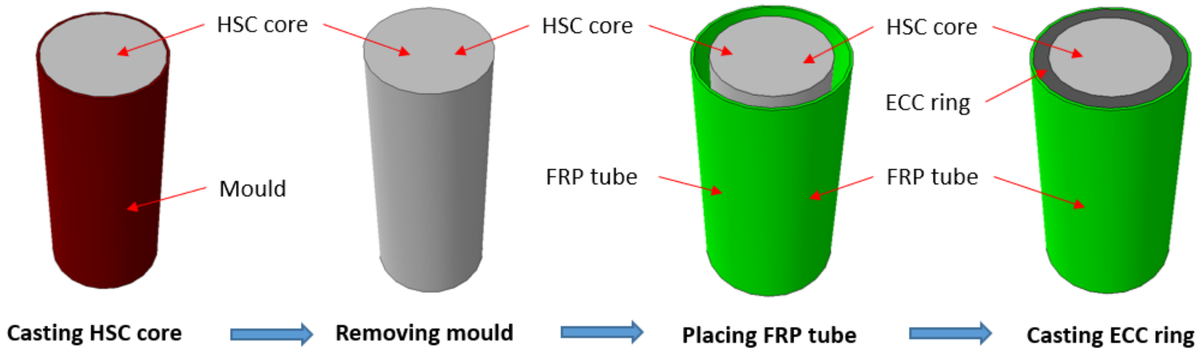

(a) Manufacturing process of FRP-ECC-HSC composite columns in laboratory

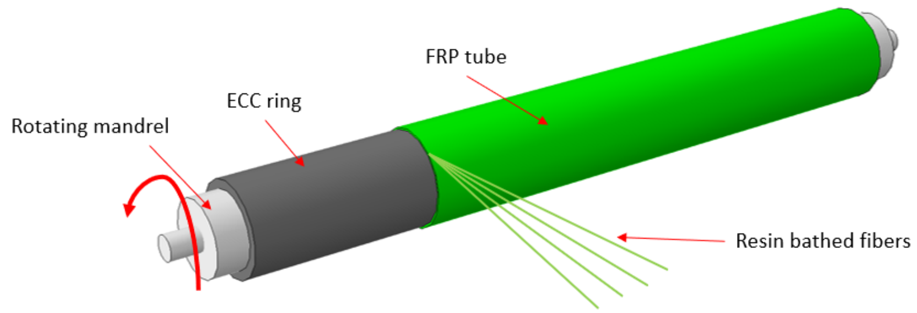

Pre-fabrication of FRP-ECC tube in factory

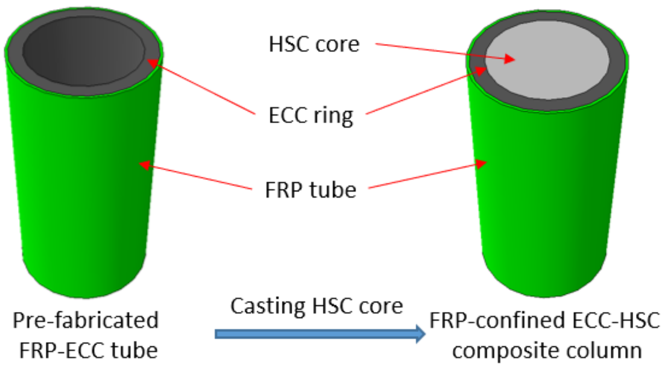

Casting HSC core in construction site

(b) Manufacturing process of FRP-ECC-HSC composite columns in engineering practice

Fig. 8 Preparation procedures for FRP-ECC-HSC composite columns

FRP-ECC-HSC ECC ring FRP-ECC ECC-HSC

Fig. 9 Different types of specimens

(a) Test setup

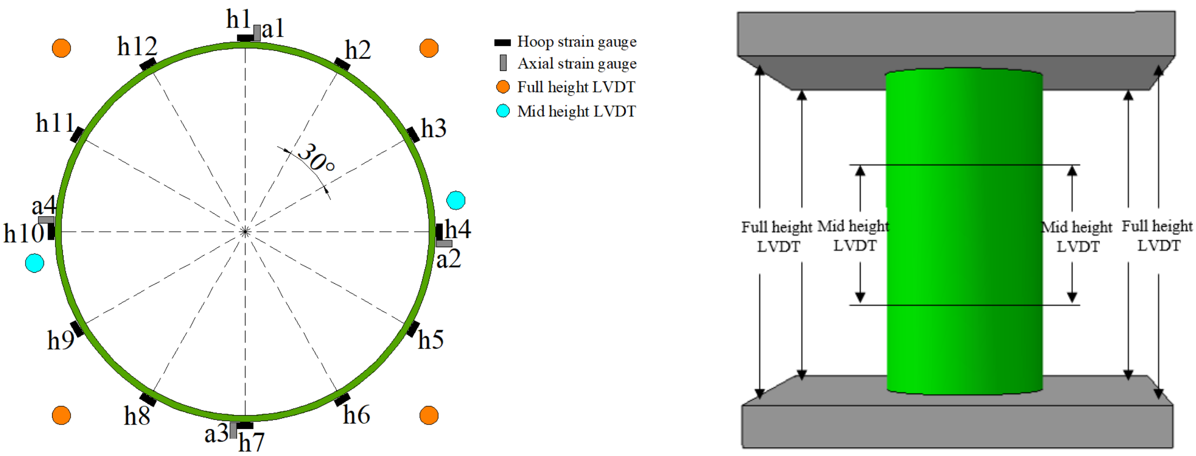

(b) Instrumentation of specimen

Fig. 10 Test setup and instrumentation

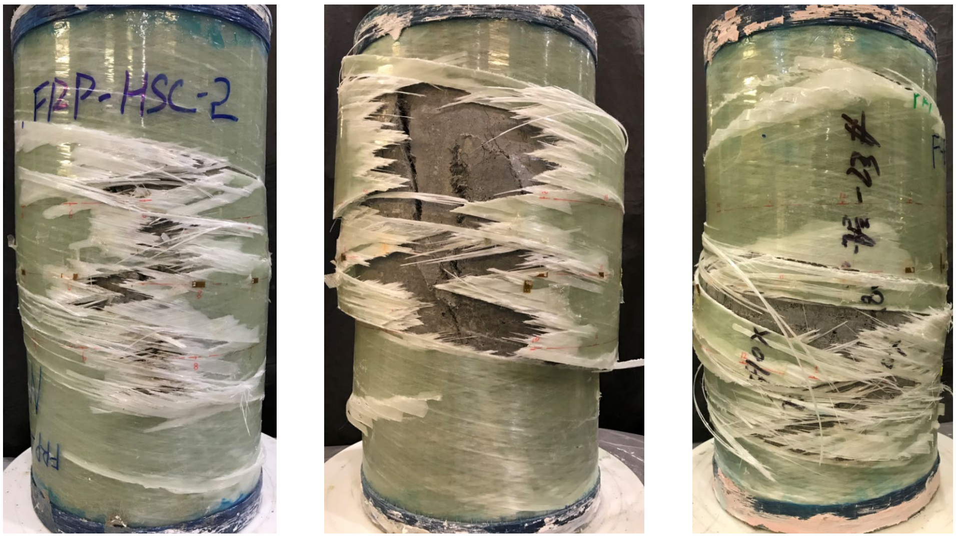

(a) FH70 (b) FE50H70-15 (c) FE50H70-25

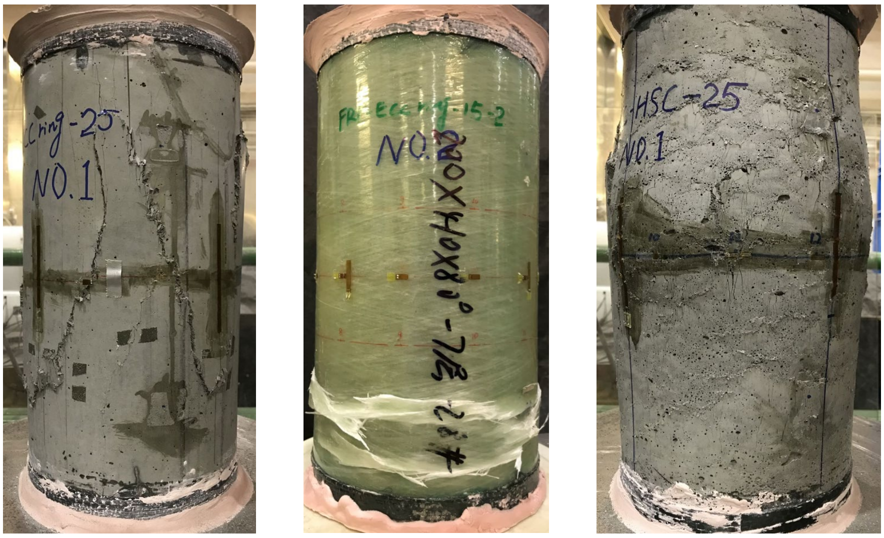

(d) E50-25 (e) FE50-15 (f) E50H70-25

Fig. 11 Typical failed specimens

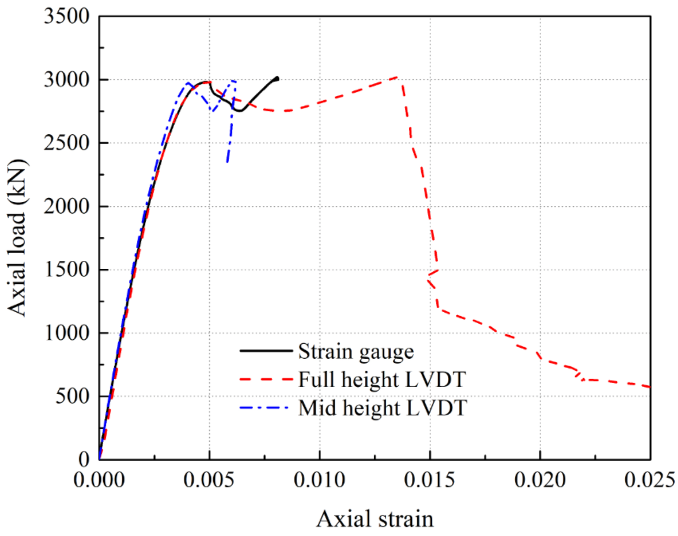

Fig. 12 Comparison of axial strain obtained by different measuring methods

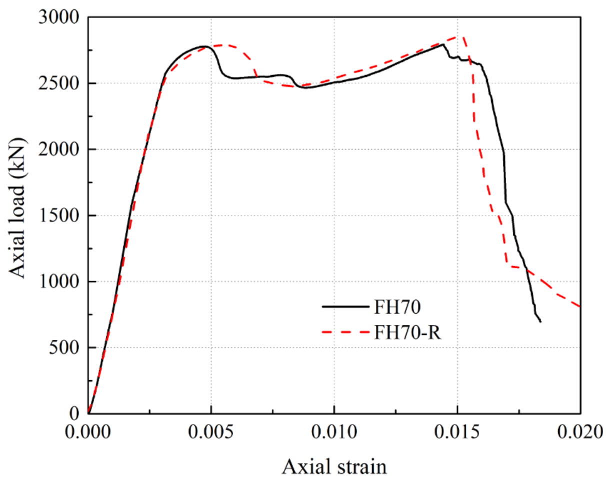

(a) FRP-confined HSC70

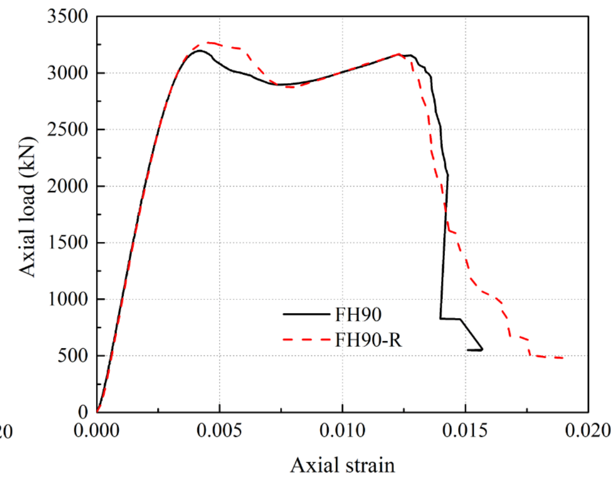

(b) FRP-confined HSC90

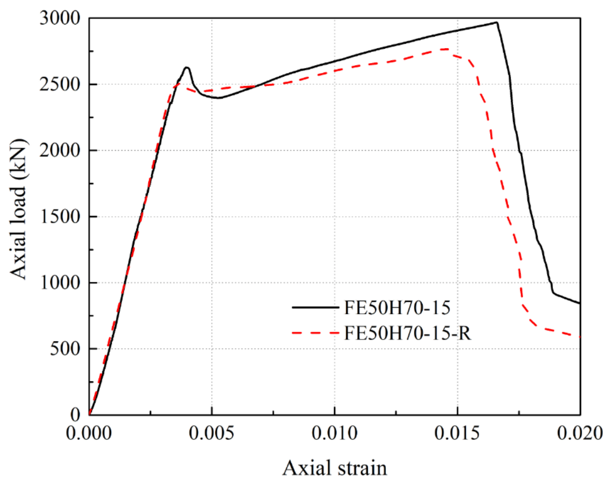

(c) FRP-ECC50-HSC70-15

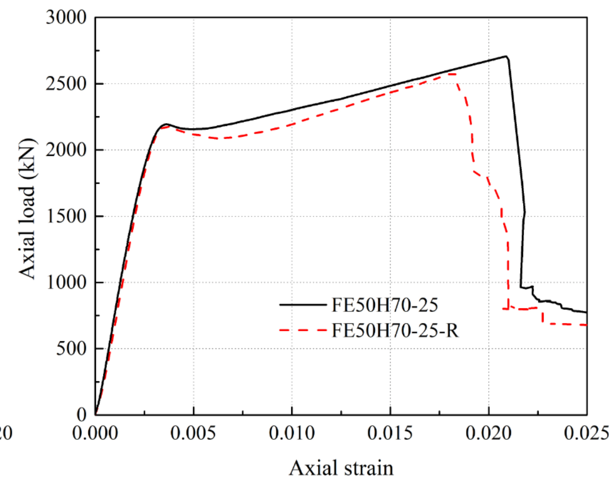

(d) FRP-ECC50-HSC70-25

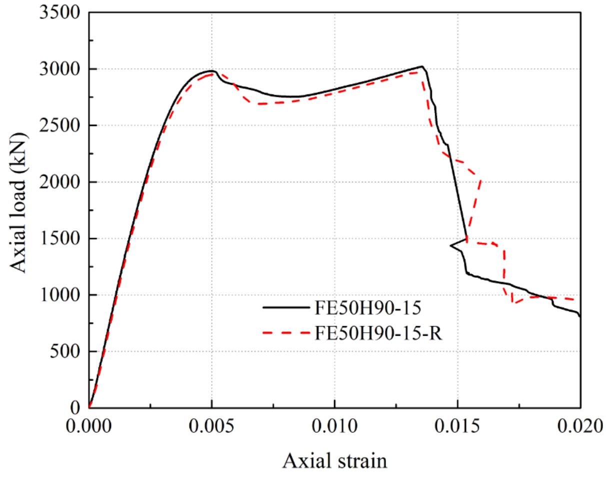

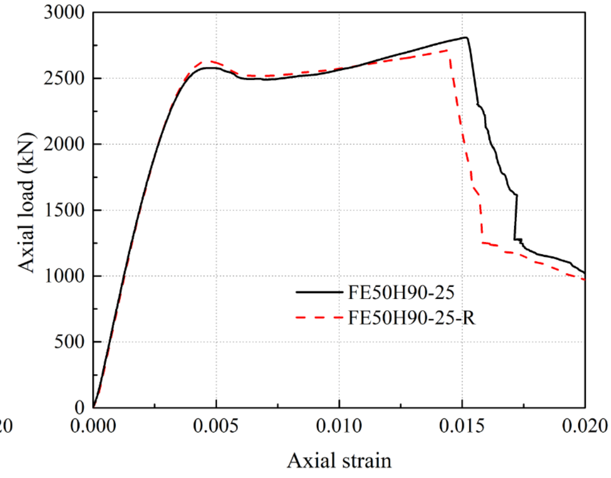

(e) FRP-ECC50-HSC90-15

(f) FRP-ECC50-HSC90-25

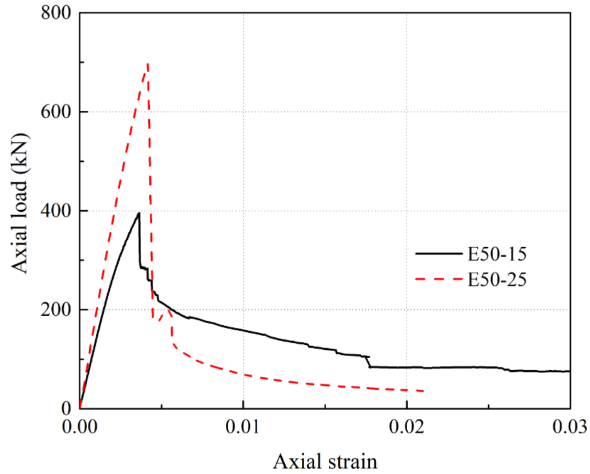

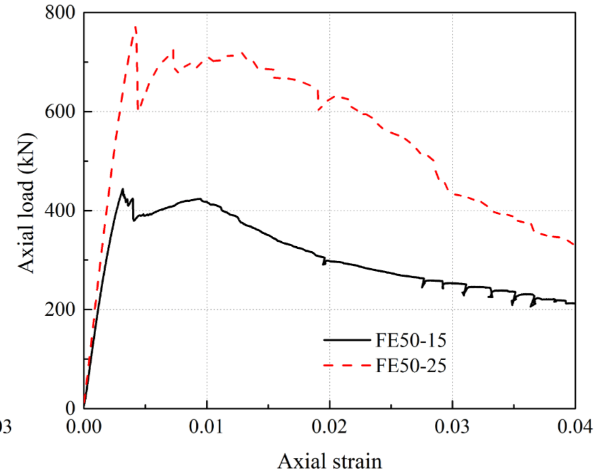

(g) ECC ring

(h) FRP-confined ECC ring

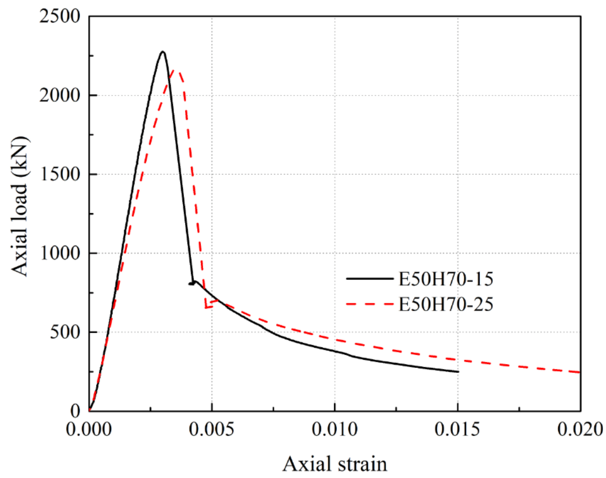

(i) ECC-confined HSC

Fig. 13 Axial load-axial strain curves of specimens

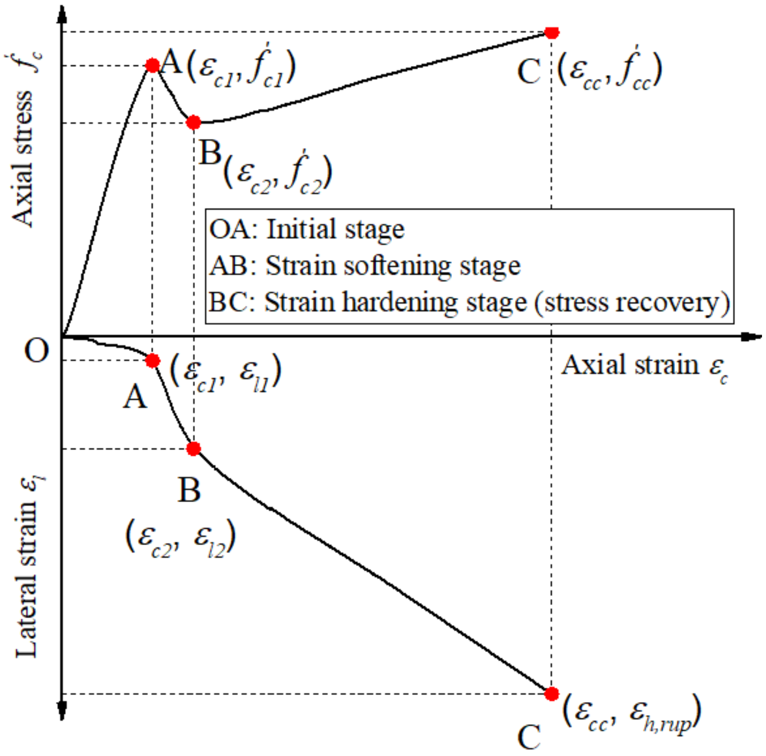

Fig. 14 Typical compressive behavior of FRP-confined HSC

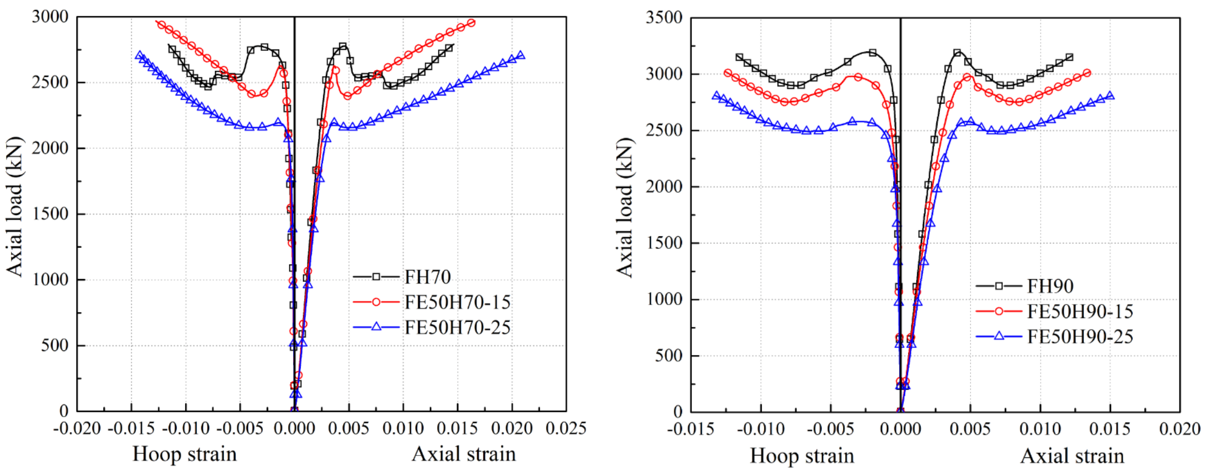

(a) C70 as HSC core (b) C90 as HSC core

Fig. 15 Typical compressive behavior of FRP-confined HSC and FRP-ECC-HSC specimens

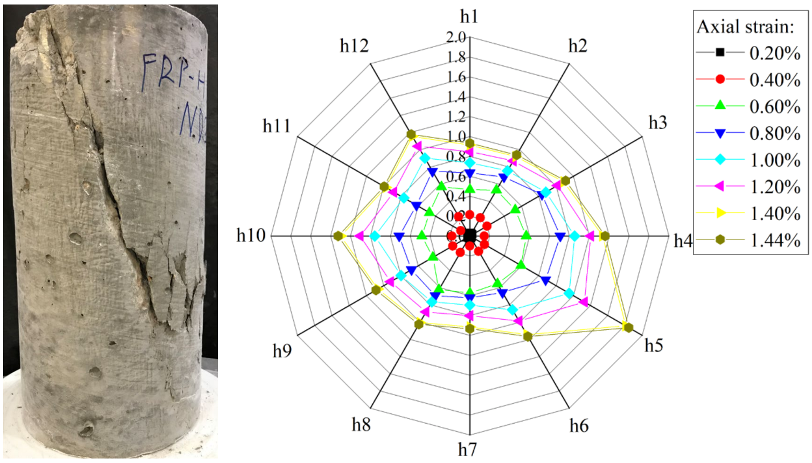

(a) FH70 (Strain unit: %)

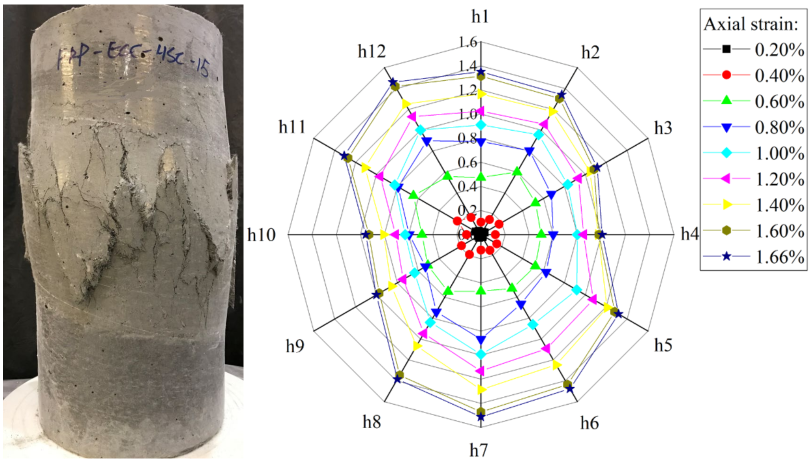

(b) FE50H70-15 (Strain unit: %)

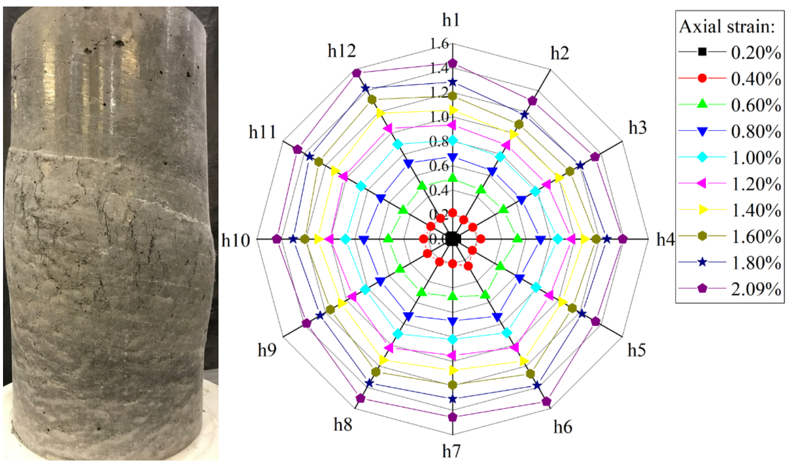

(c) FE50H70-25 (Strain unit: %)

Fig. 16 Cracking and hoop strain distribution behavior of typical specimens

Fig. 17 Crushing of HSC core

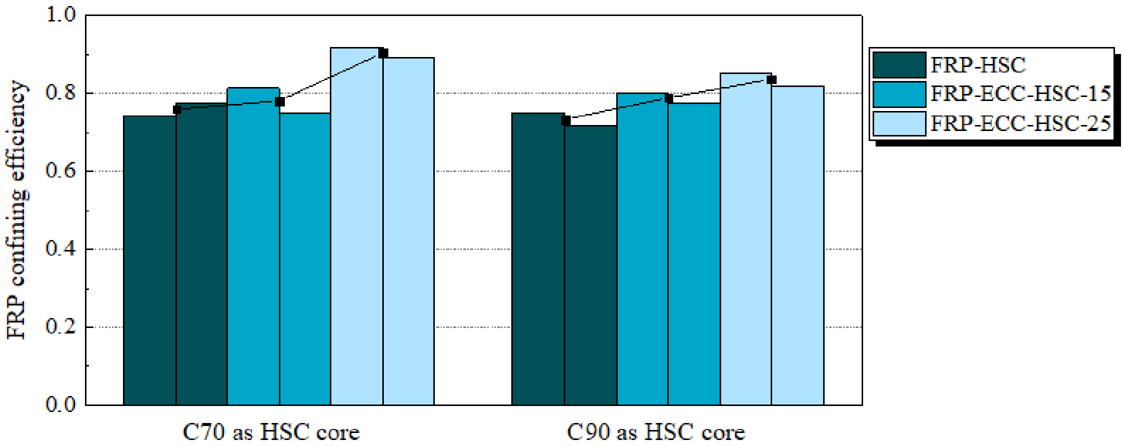

Fig. 18 FRP-confining efficiency for tested specimens

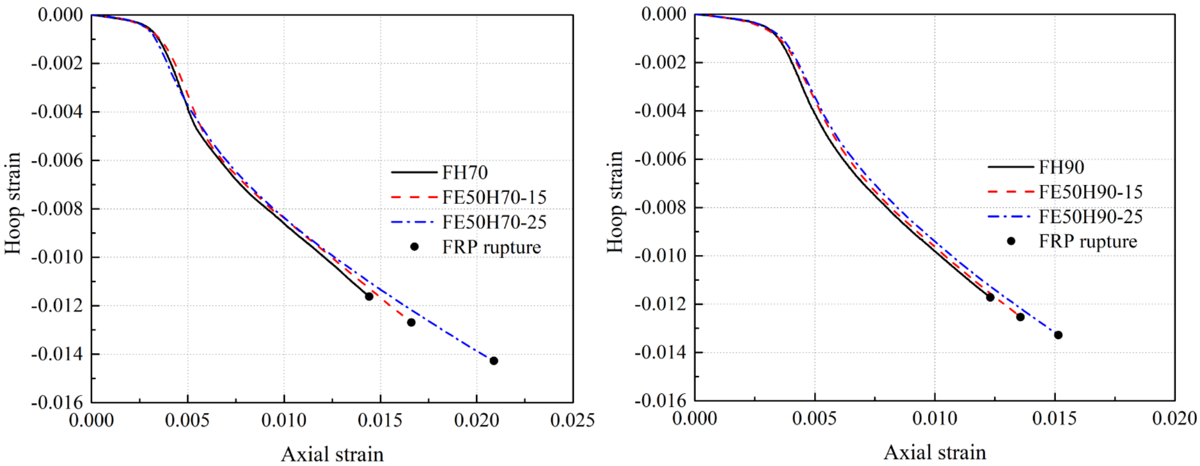

(a) C70 as HSC core (b) C90 as HSC core

Fig. 19 Typical hoop strain-axial strain relationships

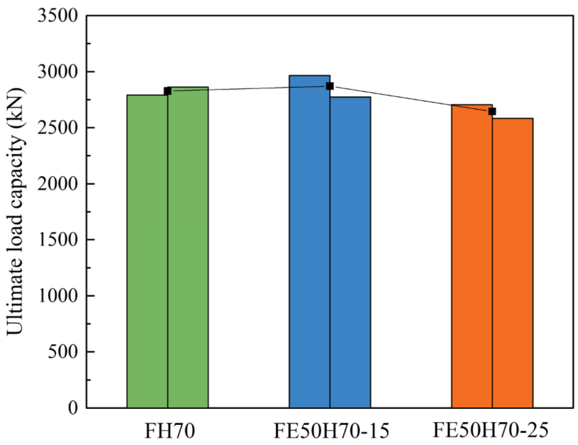

C70 as HSC core

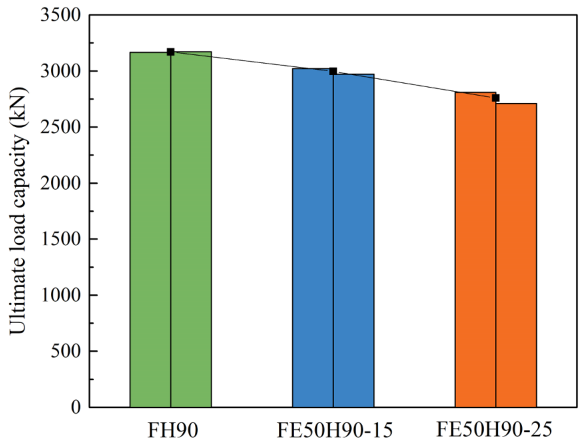

C90 as HSC core

(a) Ultimate axial load

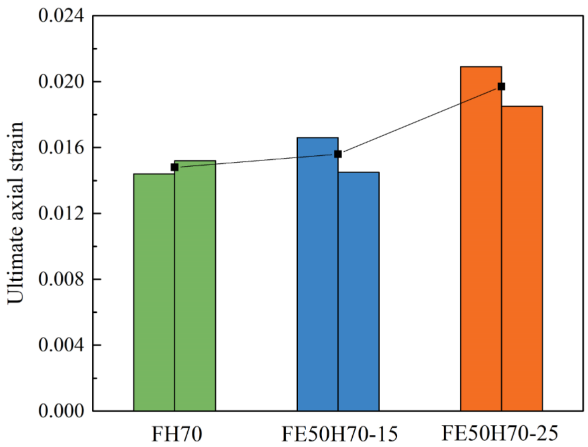

C70 as HSC core

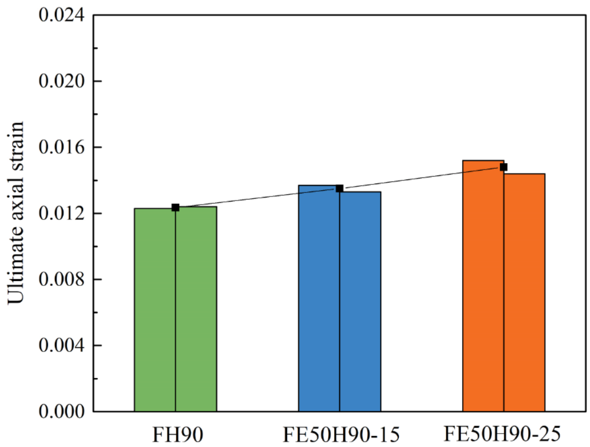

C90 as HSC core

(b) Ultimate axial strain

Fig. 20 Comparisons of axial load and axial strain at ultimate conditions

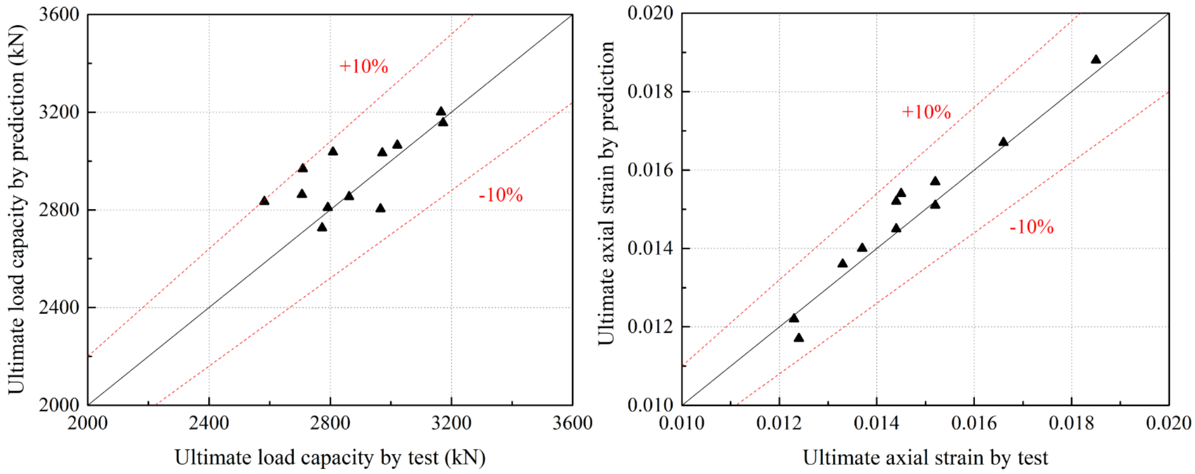

(a) Ultimate load capacity (b) Ultimate axial strain

Fig. 21 Comparison of ultimate conditions between test results and model predictions

Table 1 HSC mix proportions (kg/m^3)

HSC grade	W/C ratio	Water	Cement	Sand	Agg-10	Agg-20	S.P.*
C70	0.24	133	550	693	410	613	8.8
C90	0.20	120	603	693	410	613	10.6

S.P.*: Super plasticizer.

Table 2 ECC mix proportions (kg/m^3)

ECC grade	Water	Cement	Sand	Fly ash	S.P.	Fiber
ECC50	310.5	554.4	443.7	665.2	13.5	19.4

Table 3 Properties of polyethylene (PE) fiber

Length (mm)	Diameter (μm)	Tensile strength (MPa)	Elastic modulus (GPa)	Density (g/cm^3)
12	24	3000	120	0.97

Table 4 Specimen details

Specimen ID	HSC core		ECC ring
	Grade	Diameter (mm)	Thickness (mm)
FE50H70-15 (-R)	C70	170	15
FE50H70-25 (-R)	C70	150	25
FE50H90-15 (-R)	C90	170	15
FE50H90-25 (-R)	C90	150	25
FH70 (-R)	C70	200	-
FH90 (-R)	C90	200	-
E50-15	-	-	15
E50-25	-	-	25
FE50-15	-	-	15
FE50-25	-	-	25
E50H70-15	C70	170	15
E50H70-25	C70	150	25

Table 5 Major characteristics for tested specimens

Specimen ID	F_1 (kN)	F_2 (kN)	F_c (kN)	F_2/F_1	F_c/F_1	ε_{cc}	$\varepsilon_{h,rup}$	k_ε
FH70	2777.1	2536.3	2791.9	0.91	1.01	0.0144	0.0116	74.4%
FH70-R	2786.3	2475.0	2862.3	0.89	1.03	0.0152	0.0121	77.6%
FE50H70-15	2626.6	2396.0	2966.0	0.91	1.13	0.0166	0.0127	81.4%
FE50H70-15-R	2506.2	2443.9	2773.3	0.97	1.11	0.0145	0.0117	75.0%
FE50H70-25	2193.7	2086.8	2706.5	0.95	1.23	0.0209	0.0143	91.7%
FE50H70-25-R	2177.7	2156.9	2582.5	0.99	1.19	0.0185	0.0139	89.1%
FH90	3195.2	2897.7	3165.5	0.91	0.99	0.0123	0.0117	75.0%
FH90-R	3266.9	2873.2	3172.3	0.88	0.97	0.0124	0.0112	71.8%
FE50H90-15	2979.9	2753.7	3021.3	0.92	1.01	0.0137	0.0125	80.1%
FE50H90-15-R	2954.9	2689.3	2972.0	0.91	1.01	0.0133	0.0121	77.6%
FE50H90-25	2578.5	2519.8	2809.2	0.98	1.09	0.0152	0.0133	85.3%
FE50H90-25-R	2630.4	2494.5	2709.5	0.95	1.03	0.0144	0.0128	82.1%
E50-15	395.2	-	-	-	-	-	-	-
E50-25	697.3	-	-	-	-	-	-	-
FE50-15	443.7	379.6	423.8	0.86	0.96	0.0094	-	-
FE50-25	772.8	599.4	723.9	0.78	0.94	0.0073	-	-
E50H70-15	2276.0	-	-	-	-	-	-	-
E50H70-25	2172.7	-	-	-	-	-	-	-

Table 6 Comparison between predictions and test results

Specimen ID	Ultimate load capacity (kN)			Ultimate axial strain		
	$F_{c,test}$	$F_{c,pred}$	$F_{c,test}/F_{c,pred}$	$\varepsilon_{cc,test}$	$\varepsilon_{cc,pred}$	$\varepsilon_{cc,test}/\varepsilon_{cc,pred}$
FH70	2791.9	2809.9	0.99	0.0144	0.0145	0.99
FH70-R	2862.3	2853.8	1.00	0.0152	0.0151	1.01
FE50H70-15	2966.0	2804.7	1.06	0.0166	0.0167	1.00
FE50H70-15-R	2773.3	2726.1	1.02	0.0145	0.0154	0.94
FE50H70-25	2706.5	2863.4	0.95	0.0209	0.0194	1.08

FE50H70-25-R	2582.5	2834.0	0.91	0.0185	0.0188	0.98
FH90	3165.5	3200.7	0.99	0.0123	0.0122	1.01
FH90-R	3172.3	3156.8	1.00	0.0124	0.0117	1.06
FE50H90-15	3021.3	3065.1	0.99	0.0137	0.0140	0.98
FE50H90-15-R	2972.0	3033.6	0.98	0.0133	0.0136	0.98
FE50H90-25	2809.2	3036.8	0.93	0.0152	0.0157	0.97
FE50H90-25-R	2709.5	2968.3	0.91	0.0144	0.0152	0.95
Mean			0.98			1.00
CoV			0.044			0.039